

DSCC2013-3830

DIGITAL EFFECTS AND DELAYS IN CONNECTED VEHICLES: LINEAR STABILITY AND SIMULATIONS

Wubing B. Qin

Department of Mechanical Engineering
University of Michigan
Ann Arbor, Michigan 48109
Email: wubing@umich.edu

Gábor Orosz

Department of Mechanical Engineering
University of Michigan
Ann Arbor, Michigan 48109
Email: orosz@umich.edu

ABSTRACT

To improve the ride quality in connected vehicle platoons, information about the motion of the leader can be transmitted using vehicle-to-vehicle (V2V) communication and such information can be incorporated in the controllers of the following vehicle. However, according to the current V2V standards, dedicated short range communication (DSRC) devices transmit information every 100 ms which introduces time delays into the control loops. In this paper we study the effects of these time delays on the dynamics of vehicle platoons subject to digital control and derive conditions for plant stability and string stability. It is shown that when the time delay exceeds a critical value, no gain combination can stabilize the system. Our results have important implications on connected vehicle design.

INTRODUCTION

Recent decades have witnessed a growing interests in increasing the safety and throughput of vehicular traffic by using different control strategies [1]. One way to achieve this goal is improving the performance of autonomous cruise control (ACC) [2,3] devices by incorporating signals received from other vehicles via vehicle-to-vehicle (V2V) communication [4]. This is often referred as cooperative autonomous cruise control (CACC) [5]. Indeed these controllers use finite sampling time. For standard (radar-based) ACC the sampling time is in the range of 50 ms but dedicated short range communication devices (DSRC) only broadcast a packet every 100ms and the effective sampling time may be multiples of this when packets are lost [4]. When combining this with the zero-order hold (ZOH) [6] used in digital controllers, a hybrid system is obtained where the continuous-time dynamics is subject to piece-wise constant inputs. This in-

troduces time-dependent time delays into the vehicle dynamics [7] that can significantly influence the limitations of the controllers.

In this paper we investigate a nonlinear physics-based model that is controlled by a nonlinear digital controller [8]. Of particular interest is the stability of the system. Apart from the ability to be able to follow a leader traveling with a constant speed (called plant stability) we also require attenuations of disturbances along platoons (called string stability [9]) in order to ensure smooth traffic flow. Here, for the first time, we derive such conditions for digitally controlled vehicles by transforming the continuous-time system to a discrete time system with discrete delay. We analyze the dynamics at the linear level in the vicinity of the uniform flow equilibrium and draw stability charts for the plant and string stability of the system which can inform designers how to select feedback gains. Our results indicate that the digital effects have significant impacts on the available control gains and there exists a critical sampling time, beyond which no gain combinations can be found that ensure string stability. We validate our linear design by numerical simulations using the nonlinear model.

NONLINEAR CAR-FOLLOWING MODEL

In this section, we construct a nonlinear vehicle model and propose a nonlinear controller that can maintain a desired distance-dependent equilibrium velocity. To model the longitudinal vehicle dynamics, we consider no slip condition on the wheels and neglect the flexibility of the tires and the suspension which results in

$$m_{\text{eff}}\ddot{v} = -mg \sin \phi - \gamma mg \cos \phi - k(v + v_w)^2 + \frac{\eta}{R} T_{\text{en}}, \quad (1)$$

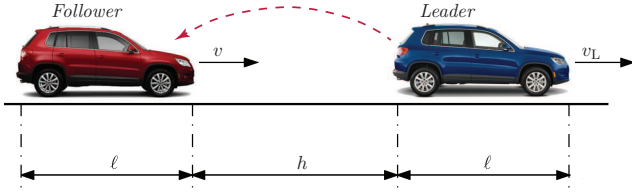


Figure 1. SEQUENCE OF CARS ON A SINGLE LANE SHOWING VEHICLES' VELOCITIES AND THE HEADWAY. THE DASHED ARROW INDICATES THE WIRELESS COMMUNICATION LINK BETWEEN VEHICLES.

where $m_{\text{eff}} = m + J/R^2$ is the effective mass, containing the mass of vehicle m , the moment of inertia J of the rotating elements, and the wheel radius R . Also, g is gravitational constant, ϕ is the inclination angle, γ is the rolling resistance coefficient, k is the air drag constant, v_w is the velocity of the head wind, η is the gear ratio. The engine torque is denoted by T_{en} which is commanded based on the distance between vehicles called headway h , the leader's velocity v_L , and the vehicle's own velocity v ; see Fig. 1. Indeed, one may add more vehicles to the platoon but the fundamental dynamics can be concluded from two consecutive vehicles [9]. We propose the nonlinear PID-type controller

$$\begin{aligned} T_{\text{en}} &= K_p \dot{\varepsilon} + K_i \varepsilon + K_v (W(v_L) - v), \\ \dot{\varepsilon} &= V(h) - v, \end{aligned} \quad (2)$$

where $V(h) - v$ represents the error between the desired distance-dependent velocity $V(h)$ and the actual velocity v of the vehicle. The function $V(h)$ is called the range policy which must satisfy the following general properties:

- (i) $V(h)$ is continuous and monotonously increasing (the more sparse traffic is, the faster the driver wants to travel);
- (ii) $V(h) \equiv 0$ for $h \leq h_{\text{st}}$ (in dense traffic, drivers intend to stop);
- (iii) $V(h) \equiv v_{\text{max}}$ for $h \geq h_{\text{go}}$ (in very sparse traffic, drivers intend to drive with maximum speed—often called free flow speed).

In this paper we choose the smooth range policy

$$V(h) = \begin{cases} 0 & \text{if } h < h_{\text{st}}, \\ \frac{v_{\text{max}}}{2} \left(1 - \cos \left(\pi \frac{h - h_{\text{st}}}{h_{\text{go}} - h_{\text{st}}} \right) \right) & \text{if } h_{\text{st}} \leq h \leq h_{\text{go}}, \\ v_{\text{max}} & \text{if } h > h_{\text{go}}, \end{cases} \quad (3)$$

shown in the left panel of Fig. 2. Moreover, the saturation function

$$W(v_L) = \begin{cases} v_L & \text{if } v_L \leq v_{\text{max}}, \\ v_{\text{max}} & \text{if } v_L > v_{\text{max}}, \end{cases} \quad (4)$$

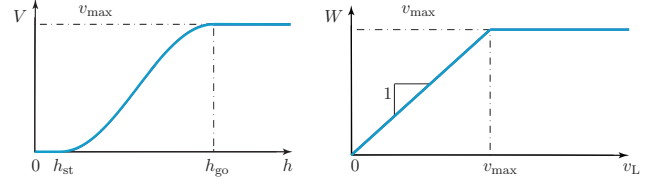


Figure 2. RANGE POLICY (3) AND SATURATION FUNCTION (4).

shown in the right panel of Fig. 2 describes the switching between ACC mode $v_L \leq v_{\text{max}}$ and normal cruise control mode.

In order to simplify the forthcoming analysis, we set $\phi = 0$ and $v_w = 0$, which means that the car is moving on a flat road with no head wind. In addition, the rotation inertia is neglected, i.e., $J = 0$, which implies $m_{\text{eff}} = m$. The other parameters are chosen based on a real vehicle; see Appendix A. Using the vehicle model (1) and controller (2), the closed loop continuous-time nonlinear model can be written as

$$\begin{cases} \dot{h} = v_L - v, \\ \dot{v} = -\gamma g - \frac{k}{m} v^2 + \hat{K}_p \dot{\varepsilon} + \hat{K}_i \varepsilon + \hat{K}_v (W(v_L) - v), \\ \dot{\varepsilon} = V(h) - v, \end{cases} \quad (5)$$

where the scaled gains are

$$\hat{K}_p = \frac{K_p \eta}{mR}, \quad \hat{K}_i = \frac{K_i \eta}{mR}, \quad \hat{K}_v = \frac{K_v \eta}{mR}. \quad (6)$$

Note that \hat{K}_p and \hat{K}_v are measured in $1/s$, \hat{K}_i is measured in $1/s^2$, and \hat{K}_p/\hat{K}_i represents the characteristic time needed to make the steady state error zero. For $v_L \leq v_{\text{max}}$ (ACC mode), system (5) possesses the equilibrium

$$v^* = v_L^*, \quad v^* = V(h^*), \quad \varepsilon^* = \frac{1}{\hat{K}_i} \left(\gamma g + \frac{k}{m} (v^*)^2 \right). \quad (7)$$

This is often called the uniform flow equilibrium of vehicular platoons [1] referring to the situation when equidistant vehicles travel with the same velocity. Our goal is to design a controller to ensure that the system can reach this equilibrium (i.e., plant stability is satisfied) and can also attenuate perturbations introduced by the leader (i.e., string stability holds) [9].

SEMI-DISCRETIZATION AND LINEARIZATION

In this section, we semi-discretize the continuous-time nonlinear model (5), that is, we create a nonlinear hybrid system: a continuous-time system subject to piece-wise constant control inputs. We also linearize this system to allow further analysis of the dynamics.

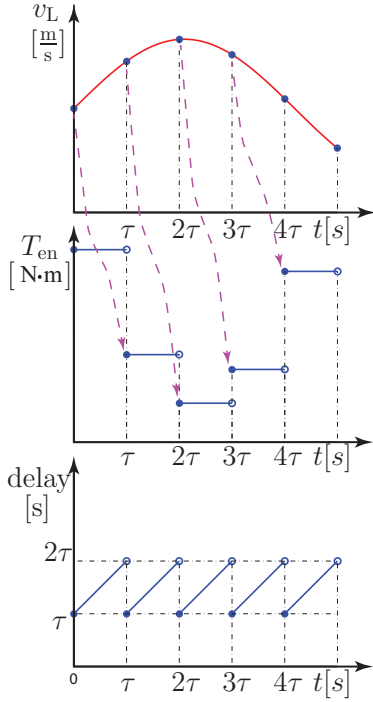


Figure 3. LEADER'S VELOCITY, TORQUE COMMAND AND DELAY VARIATIONS AS A FUNCTION OF TIME. TOP ROW: LEADER'S VELOCITY IS SAMPLED EVERY τ TIME. MIDDLE ROW: CONTROLLER OUTPUT AT $t = t_k$ BASED ON THE INFORMATION OF $t = t_{k-1}$. BOTTOM: TIME DELAY IN THIS SAMPLE-CONTROL MECHANISM.

Let us denote the discretization unit (sampling time) as τ and define the time mesh $t_k = k\tau$, $k = 0, 1, 2, \dots$. As shown in the top panel of Fig. 3, the controller samples the leader's velocity (as well as its own velocity and the headway) at each t_{k-1} and then outputs a torque command at $t = t_k$ based on the information obtained at $t = t_{k-1}$. The torque is kept constant until $t = t_{k+1}$, which is known as ZOH in digital control [6]; see the middle panel of Fig. 3. This means that the effective delay increases from τ to 2τ during each sampling interval as shown in the bottom panel of Fig. 3. The average delay is $3\tau/2$ that may be used to approximate the delay effects; see [10, 11]. Note that the physical part of the model still evolves in continuous time. Thus, the digitally controlled system can be written as

$$\begin{cases} \dot{h} = v_L - v, \\ \dot{v} = -\gamma g - \frac{k}{m}v^2 + \hat{K}_p(V(h(k-1)) - v(k-1)) \\ \quad + \hat{K}_i\varepsilon(k-1) + \hat{K}_v(v_L(k-1) - v(k-1)), \\ \dot{\varepsilon} = V(h) - v, \end{cases} \quad t_k \leq t < t_{k+1}, \quad (8)$$

cf. (5). Here we introduced the notation $h(k) = h(t_k)$, $v(k) = v(t_k)$, $\varepsilon(k) = \varepsilon(t_k)$ and $v_L(k) = v_L(t_k)$, while h , v , ε and v_L without arguments represent continuous-time variables.

Solving the differential equation (8) on the time interval $[t_k, t_{k+1})$ one may create a discrete map, that is, fully discretize the dynamics. However, this is a difficult task due to the nonlinearities in the system. Therefore, we linearize the system about the equilibrium (7) and discretize the obtained linear equations. Defining the perturbations $\tilde{h} = h - h^*$, $\tilde{v} = v - v^*$, $\tilde{\varepsilon} = \varepsilon - \varepsilon^*$ and $\tilde{v}_L = v_L - v_L^*$, one may obtain

$$\begin{bmatrix} \dot{\tilde{h}} \\ \dot{\tilde{v}} \\ \dot{\tilde{\varepsilon}} \end{bmatrix} = \begin{bmatrix} 0 & -1 & 0 \\ 0 & -2\frac{k}{m}v^* & 0 \\ N_* & -1 & 0 \end{bmatrix} \begin{bmatrix} \tilde{h} \\ \tilde{v} \\ \tilde{\varepsilon} \end{bmatrix} + \begin{bmatrix} 1 \\ 0 \\ 0 \end{bmatrix} \tilde{v}_L + \begin{bmatrix} 0 \\ \hat{K}_v \\ 0 \end{bmatrix} \tilde{v}_L(k-1) \\ + \begin{bmatrix} 0 & 0 & 0 \\ \hat{K}_p N_* & -(\hat{K}_p + \hat{K}_v) & \hat{K}_i \\ 0 & 0 & 0 \end{bmatrix} \begin{bmatrix} \tilde{h}(k-1) \\ \tilde{v}(k-1) \\ \tilde{\varepsilon}(k-1) \end{bmatrix}, \quad t_k \leq t < t_{k+1}, \quad (9)$$

where

$$N_* = V'(h^*) = \begin{cases} 0 & \text{if } h < h_{st}, \\ \frac{\pi}{2} \frac{v_{\max}}{h_{go} - h_{st}} \sin\left(\pi \frac{h^* - h_{st}}{h_{go} - h_{st}}\right) & \text{if } h_{st} \leq h \leq h_{go}, \\ 0 & \text{if } h > h_{go}, \end{cases} \quad (10)$$

which is equivalent to

$$N_* = V'(V^{-1}(v^*)) = \begin{cases} 0 & \text{if } h < h_{st}, \\ \frac{\pi \sqrt{v^*(v_{\max} - v^*)}}{h_{go} - h_{st}} & \text{if } h_{st} \leq h \leq h_{go}, \\ 0 & \text{if } h > h_{go}. \end{cases} \quad (11)$$

PLANT STABILITY AND STRING STABILITY FOR DIGITALLY CONTROLLED PLATOONS

In this section, we fully discretize the linear system (9) by solving it on the time interval $[t_k, t_{k+1})$ and create a discrete-time map. Then we adopt the concepts of plant stability and string stability that have been used before for continuous-time systems [9]. We also demonstrate the results by numerical simulations using the nonlinear model (8).

Plant stability means that when the leader is driving at a constant velocity $v_L(t) \equiv v^*$, (i.e., $\tilde{v}_L(t) \equiv 0$), then the follower's velocity approaches the leader's velocity. On the other hand, string stability also requires that fluctuations in the leader's velocity are attenuated as they propagate along the platoon. According to Fourier's theory, periodic signals can be written as the infinite sum of sines and cosines and this can also be extended to non-periodic functions that are quadratic integrable. Thus, for linear systems attenuation of sines and cosines at all frequencies is adequate for string stability. Moreover, as there is just a phase

difference in cosine and sine, the string stability condition is simplified to attenuation of the sine input

$$v_L(t) = v_L^* + v_L^{\text{amp}} \sin(\omega t) \Rightarrow \tilde{v}_L(t) = v_L^{\text{amp}} \sin(\omega t), \quad (12)$$

at all frequencies $\omega > 0$.

Solving the linear equation (9) with periodic input (12) on the interval $[t_k, t_{k+1})$, one may derive the discrete-time map

$$\begin{aligned} \mathbf{x}(k+1) &= \mathbf{A}\mathbf{x}(k) + \mathbf{B}\mathbf{u}(k), \\ \mathbf{y}(k) &= \mathbf{C}\mathbf{x}(k), \end{aligned} \quad (13)$$

where the state and the output are defined as

$$\mathbf{x}(k) = \begin{bmatrix} \tilde{h}(k) \\ \tilde{v}(k) \\ \tilde{\varepsilon}(k) \\ \tilde{h}(k-1) \\ \tilde{v}(k-1) \\ \tilde{\varepsilon}(k-1) \end{bmatrix}, \quad \mathbf{y}(k) = \tilde{v}(k), \quad (14)$$

the input becomes

$$\mathbf{u}(k) = \begin{bmatrix} \tilde{v}_{L_1}(k) \\ \tilde{v}_{L_2}(k) \end{bmatrix} = \begin{bmatrix} v_L^{\text{amp}} \sin((k-1)\omega\tau) \\ v_L^{\text{amp}} \cos((k-1)\omega\tau) \end{bmatrix}, \quad (15)$$

and the matrices can be written as

$$\begin{aligned} \mathbf{A} &= \begin{bmatrix} 1 & -\alpha_4 & 0 & \alpha_3 \hat{K}_p N_* & -\alpha_3(\hat{K}_p + \hat{K}_v) & \alpha_3 \hat{K}_i \\ 0 & e^{-\alpha_0 \tau} & 0 & \alpha_4 \hat{K}_p N_* & -\alpha_4(\hat{K}_p + \hat{K}_v) & \alpha_4 \hat{K}_i \\ N_* \tau & \alpha_2 & 1 & \alpha_1 \hat{K}_p N_* & -\alpha_1(\hat{K}_p + \hat{K}_v) & \alpha_1 \hat{K}_i \\ 1 & 0 & 0 & 0 & 0 & 0 \\ 0 & 1 & 0 & 0 & 0 & 0 \\ 0 & 0 & 1 & 0 & 0 & 0 \end{bmatrix}, \\ \mathbf{B} &= \begin{bmatrix} \alpha_3 \hat{K}_v + \beta_1 & \beta_2 \\ \alpha_4 \hat{K}_v & 0 \\ \alpha_1 \hat{K}_v + \beta_3 & \beta_4 \\ 0 & 0 \\ 0 & 0 \\ 0 & 0 \end{bmatrix}, \quad \mathbf{C} = [0 \quad 1 \quad 0 \quad 0 \quad 0 \quad 0], \end{aligned} \quad (16)$$

where

$$\begin{aligned} \alpha_0 &= 2 \frac{k}{m} v^*, \\ \alpha_1 &= \frac{N_* - \alpha_0}{\alpha_0^3} (\alpha_0 \tau - 1 + e^{-\alpha_0 \tau}) - \frac{N_*}{2\alpha_0} \tau^2, \\ \alpha_2 &= \frac{\alpha_0 - N_*}{\alpha_0^2} (e^{-\alpha_0 \tau} - 1) - \frac{1}{\alpha_0} N_* \tau, \\ \alpha_3 &= \frac{1 - e^{-\alpha_0 \tau} - \alpha_0 \tau}{\alpha_0^2}, \\ \alpha_4 &= \frac{1 - e^{-\alpha_0 \tau}}{\alpha_0}, \end{aligned} \quad (17)$$

and

$$\begin{aligned} \beta_1 &= \frac{1}{\omega} (\sin(2\omega\tau) - \sin(\omega\tau)), \\ \beta_2 &= -\frac{1}{\omega} (\cos(2\omega\tau) - \cos(\omega\tau)), \\ \beta_3 &= \frac{N_*}{\omega^2} (\cos(\omega\tau) - \cos(2\omega\tau) - \omega\tau \sin(\omega\tau)), \\ \beta_4 &= \frac{N_*}{\omega^2} (\omega\tau \cos(\omega\tau) + \sin(\omega\tau) - \sin(2\omega\tau)). \end{aligned} \quad (18)$$

Note that the continuous sinusoidal signal (12) that is fed into the continuous-time system (9) is split into a sine and a cosine term in the input (15) driving the discrete-time map (13). Moreover, the state space of the continuous-time system is three dimensional while the discrete-time system has a six dimensional state space (although the rank of the system matrix is only four).

Plant Stability Analysis

In this subsection, the methodology given in [7] is used to study plant stability. In particular, we analyze (9) subject to the input $\tilde{v}_L(t) \equiv 0$ that corresponds to $\mathbf{u}(k) \equiv \mathbf{0}$ in (13). This results in a linear autonomous map with system matrix \mathbf{A} .

To ensure plant stability, all eigenvalues of the system matrix \mathbf{A} must be within the unit circle. The characteristic equation of (13) can be written as

$$\det(z\mathbf{I} - \mathbf{A}) = z^2(z^4 + a_3 z^3 + a_2 z^2 + a_1 z + a_0) := z^2 f(z) = 0, \quad (19)$$

where $z \in \mathbb{C}$, $\mathbf{I} \in \mathbb{R}^{6 \times 6}$ is the identity matrix and

$$\begin{aligned} a_3 &= -e^{-\alpha_0 \tau} - 2, \\ a_2 &= -\alpha_1 \hat{K}_i + (-\alpha_3 N_* + \alpha_4) \hat{K}_p + \alpha_4 \hat{K}_v + (2e^{-\alpha_0 \tau} + 1), \\ a_1 &= (-N_* \tau \alpha_3 + e^{-\alpha_0 \tau} \alpha_1 - \alpha_2 \alpha_4 + \alpha_1) \hat{K}_i \\ &\quad + (-2\alpha_4 + \alpha_3 N_* e^{-\alpha_0 \tau} + \alpha_4^2 N_* + \alpha_3 N_*) \hat{K}_p - 2\alpha_4 \hat{K}_v - e^{-\alpha_0 \tau}, \\ a_0 &= (-e^{-\alpha_0 \tau} \alpha_1 + \alpha_2 \alpha_4 + N_* \tau \alpha_4^2 + N_* \tau \alpha_3 e^{-\alpha_0 \tau}) \hat{K}_i \\ &\quad + (-\alpha_3 N_* e^{-\alpha_0 \tau} - \alpha_4^2 N_* + \alpha_4) \hat{K}_p + \alpha_4 \hat{K}_v. \end{aligned} \quad (20)$$

The characteristic equation (19) has a zero root with multiplicity two and the plant stability is guaranteed if the four roots of $f(z) = 0$ lie inside the unit circle in the complex plane. Stability changes when eigenvalues cross the unit circle that may happen in three principally different ways [12]:

- (i) a real eigenvalue crosses the unit circle at 1;
- (ii) a real eigenvalue crosses the unit circle at -1 ;
- (iii) a pair of complex conjugate eigenvalues crosses the unit circle at $e^{\pm i\theta}$;

which correspond to fold, flip, and Neimark-Sacker bifurcations in the corresponding nonlinear system, respectively. In parameter space the linear stability boundaries are given by

$$z = 1 \iff f_1(\hat{K}_p, \hat{K}_i, \hat{K}_v, v^*, \tau) = 0, \quad (21)$$

$$z = -1 \iff f_2(\hat{K}_p, \hat{K}_i, \hat{K}_v, v^*, \tau) = 0, \quad (22)$$

$$z = e^{i\theta} \iff \begin{cases} f_3(\hat{K}_p, \hat{K}_i, \hat{K}_v, v^*, \tau, \theta) = 0, \\ f_4(\hat{K}_p, \hat{K}_i, \hat{K}_v, v^*, \tau, \theta) = 0. \end{cases} \quad (23)$$

In (23) the real and imaginary parts have been separated. Considering fixed \hat{K}_v , v^* and τ , (21), (22) and (23) result in the stability boundaries in the (\hat{K}_i, \hat{K}_p) -plane:

$$\hat{K}_i = 0, \quad (24)$$

$$\hat{K}_p = \frac{b_{11}}{d_{10}} \hat{K}_i + \frac{b_{10}}{d_{10}}, \quad (25)$$

$$\begin{cases} \hat{K}_i = \frac{b_{23} \cos^3 \theta + b_{22} \cos^2 \theta + b_{21} \cos \theta + b_{20}}{d_{21} \cos \theta + d_{20}}, \\ \hat{K}_p = \frac{b_{33} \cos^3 \theta + b_{32} \cos^2 \theta + b_{31} \cos \theta + b_{30}}{d_{21} \cos \theta + d_{20}}, \end{cases} \quad (26)$$

respectively, where the coefficients b_{ij} and d_{ij} are defined in Appendix B.

Fig. 4 shows the (\hat{K}_i, \hat{K}_p) stability charts for different values of \hat{K}_v and τ . We consider $v^* = v_{\max}/2 = 15 \text{ m/s}$ where $N_* = \pi/2 \text{ s}^{-1}$ reaches maximum (cf. (11)). Solid red curves represent plant stability boundaries, and the lobe-shaped shaded domains (both light gray and dark gray) are plant stable. For each row, the plant stable domain shrinks as the sampling time τ increases. Still, the plant stability curve and the vertical axis enclose a plant stable domain for any positive τ . This can be proven by calculating

$$\begin{aligned} \left. \frac{d\hat{K}_i}{d\hat{K}_p} \right|_{\theta \rightarrow 0} &= \lim_{\theta \rightarrow 0} \frac{d\hat{K}_i/d\theta}{d\hat{K}_p/d\theta} \\ &= \frac{2\alpha_0 N_* (\alpha_0 + \hat{K}_v)}{2(N_* - \alpha_0)(\alpha_0 + \hat{K}_v) + 3N_* \tau \alpha_0^2 - \hat{K}_v N_* \alpha_0 \tau \coth \frac{\alpha_0 \tau}{2}}, \end{aligned} \quad (27)$$

where $\theta \rightarrow 0$ corresponds to the point where the plant stable curve emanates from the vertical axis. Notice that (27) is a positive function that decreases monotonically with τ and goes to zero as τ goes to infinity, implying the existence of a plant stable domain for any positive τ .

The critical angular frequencies at which plant stability changes can be calculated by $\Omega_{cr} = \theta/\tau$ and these are shown in Fig. 5 corresponding to the plant stability curves at the top row of Fig. 4. Oscillations with angular frequency Ω_{cr} arise when crossing a plant stability boundary (light gray to white in Fig. 4). The frequency Ω_{cr} increases monotonously along the stability boundary implying that low-frequency oscillations arise when crossing the lower part of the stability curve while crossing the upper part results in high-frequency oscillations.

To illustrate how plant stability can be lost when τ increases, the point $(\hat{K}_i, \hat{K}_p) = (4, 10)$ is marked on the first three panels in Fig. 4 denoted by A, B and C, respectively. While the system with these gains is plant stable for the continuous-time system and for the discrete-time system with small sampling time ($\tau = 0.05 \text{ s}$), it is plant unstable for larger sampling time ($\tau = 0.1 \text{ s}$). This can also be observed by looking at the top row of Fig. 6. The left panel depicts the characteristic roots for the continuous-time system: all three roots being in the left-half complex plane imply stability. The other panels show the characteristic roots of the discrete-time system given by (19). As τ is increased a complex conjugate pair of roots moves outside the unit circle leading to stability loss. One may also notice in Fig. 4, the plant stable domain increases monotonously with \hat{K}_v for the continuous-time system but this is not the case for the discrete-time system. The plant stable domain might be shifted, expanded or shrunk while increasing \hat{K}_v which warns the designers that the gains must be chosen appropriately to ensure plant stability.

To visualize the plant stability loss in the time domain, the time response of the nonlinear system (8) is shown at the bottom of Fig. 6 when the system is subjected to a constant input $v_L(t) \equiv v^*$. The time step used in the simulation is one hundredth of the sampling time τ . Observing the region marked by a cyan circle on the rightmost panel, one may notice that the time responses are not smooth at t_k corresponding to the fact the digital controller forces the system with a piece-wise constant signal; see the middle panel of Fig. 3. The larger the sampling time is, the more obvious the digital effects are, and these are responsible for the instability.

String Stability Analysis

In this subsection, we study the steady state behavior of system (9) with sinusoidal input (12) which is equivalent to investigating (13) using input (15). In particular, we use the transfer function of the discrete-time system to evaluate string stability.

For linear time invariant (LTI) systems (that are plant stable), the steady-state response to a sinusoidal input is a sinusoidal output. This holds for both continuous-time and discrete-time systems and in both cases the amplitude ratio between the output

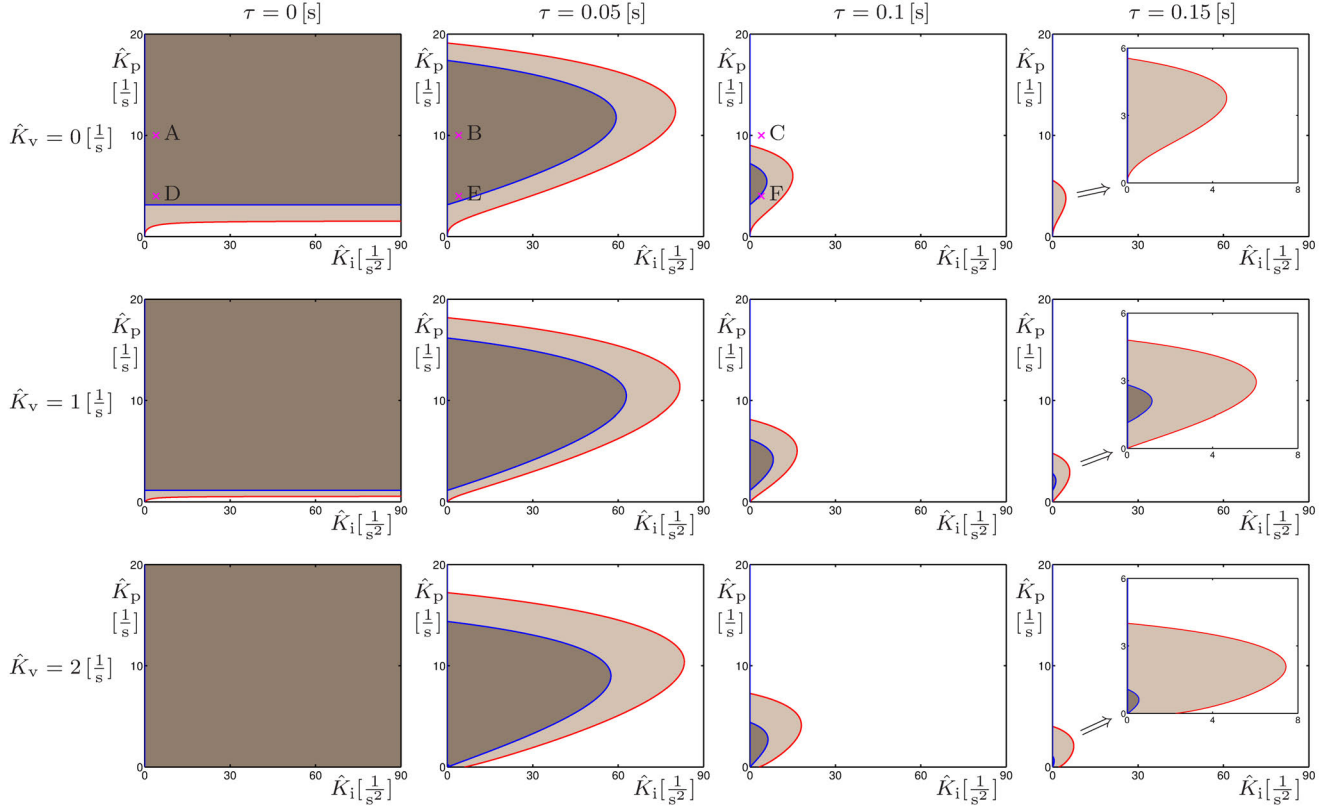


Figure 4. STABILITY DIAGRAMS IN THE (\hat{K}_i, \hat{K}_p) -PLANE FOR $v^* = 15 \text{ m/s}$ AND DIFFERENT VALUES OF \hat{K}_v AND τ AS INDICATED. RED AND BLUE CURVES CORRESPOND TO CHANGES IN PLANT AND STRING STABILITY, RESPECTIVELY. DARK GRAY REGIONS REPRESENT STRING STABLE PARAMETERS WHILE IN THE LIGHT GRAY REGIONS ONLY PLANT STABILITY IS ACHIEVED.

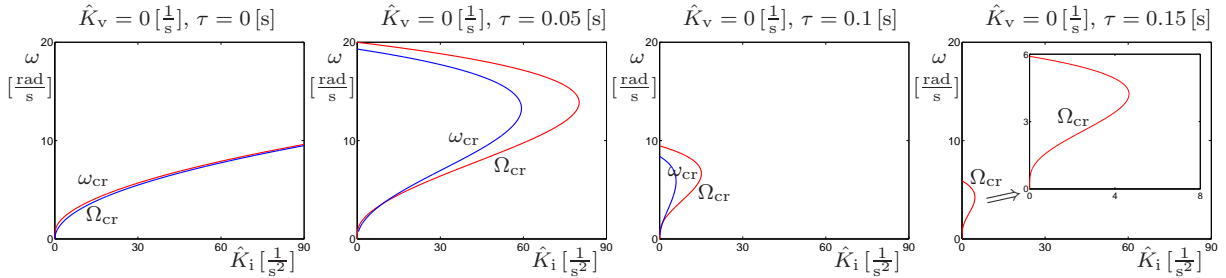


Figure 5. CRITICAL ANGULAR FREQUENCIES CORRESPONDING TO THE FIRST ROW IN Fig. 4. RED AND BLUE CURVES REPRESENT THE CRITICAL FREQUENCIES RELATED TO PLANT (Ω_{cr}) AND STRING (ω_{cr}) STABILITY, RESPECTIVELY.

and input signals can be derived using transfer functions (here denoted by Γ). In particular, for continuous-time systems the amplitude ratio is given by $|\Gamma(j\omega)|$, while for discrete-time systems by $|\Gamma(e^{j\omega\tau})|$ [6]. String stability is guaranteed if the amplitude ratio stays below 1 for all excitation frequencies $\omega > 0$.

In the discrete-time model (13), there are two inputs $\tilde{v}_{L1}(k)$, $\tilde{v}_{L2}(k)$ given by (15) and one output $y(k) = \tilde{v}(k)$. Thus,

the (vector-valued) transfer function is defined by

$$\Gamma(z) = [\Gamma_1(z) \quad \Gamma_2(z)] = \begin{bmatrix} \tilde{V}(z) & \tilde{V}(z) \\ \tilde{V}_{L1}(z) & \tilde{V}_{L2}(z) \end{bmatrix}, \quad (28)$$

where $\tilde{V}_{L1}(z)$, $\tilde{V}_{L2}(z)$ and $\tilde{V}(z)$ denote the z-transform of the inputs and the output.

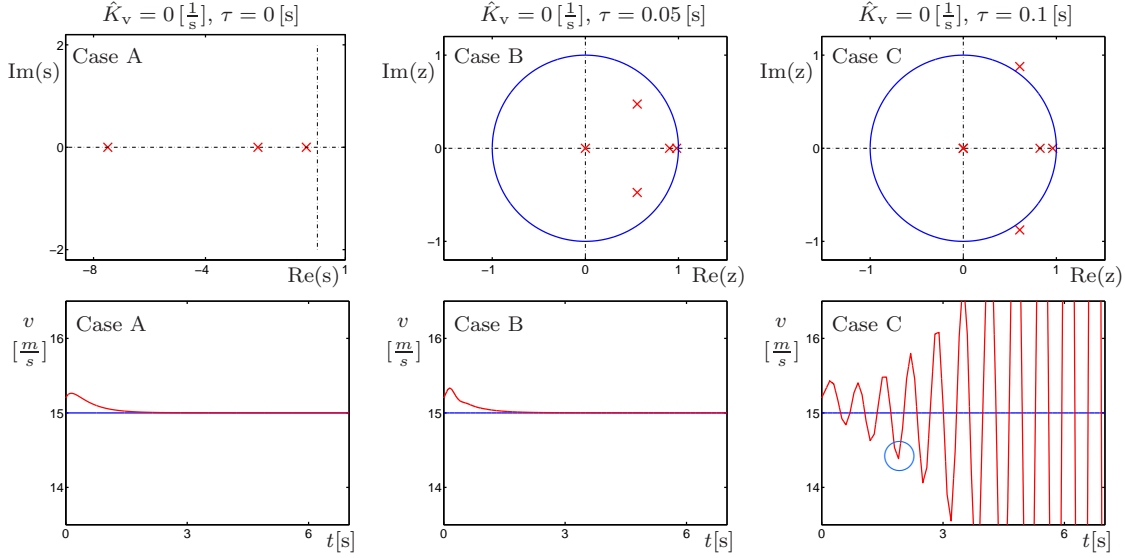


Figure 6. TOP ROW: ROOT LOCI CORRESPONDING TO THE POINTS A, B, AND C IN Fig. 4 LOCATED AT $\hat{K}_p = 10 \text{ s}^{-1}$, $\hat{K}_i = 4 \text{ s}^{-2}$. NOTE THAT THE LEFT PANEL SHOWS THE CHARACTERISTIC ROOTS OF THE CONTINUOUS-TIME SYSTEM (5) ON THE s -DOMAIN, WHILE THE RIGHT TWO PANELS SHOW THE CHARACTERISTIC ROOTS OF THE DISCRETE-TIME SYSTEM (13) ON THE z -DOMAIN. BOTTOM ROW: SIMULATIONS FOR THE NONLINEAR SYSTEM (8) SUBJECT TO CONSTANT INPUT $v_L(t) \equiv v_L^*$. THE INITIAL PERTURBATIONS ARE $\tilde{h}_0 = 0.2 \text{ m}$, $\tilde{v}_0 = 0.2 \text{ m/s}$, $\tilde{\varepsilon}_0 = 0 \text{ m/s}$. BLUE AND RED CURVES REPRESENT THE LEADER'S AND THE FOLLOWER'S VELOCITIES, RESPECTIVELY.

The transfer function can be calculated as

$$\Gamma(z) = \begin{bmatrix} \Gamma_1(z) & \Gamma_2(z) \end{bmatrix} = \mathbf{C}(z\mathbf{I} - \mathbf{A})^{-1}\mathbf{B}, \quad (29)$$

where

$$\begin{aligned} \Gamma_1(z) &= \frac{r_{13}z^3 + r_{12}z^2 + r_{11}z + r_{10}}{z^4 + a_3z^3 + a_2z^2 + a_1z + a_0}, \\ \Gamma_2(z) &= \frac{r_{21}z + r_{20}}{z^4 + a_3z^3 + a_2z^2 + a_1z + a_0}, \end{aligned} \quad (30)$$

and the denominator is indeed equal to $f(z)$ in (19) with coefficients a_3, a_2, a_1, a_0 given by (20). The coefficients of the numerators become

$$\begin{aligned} r_{10} &= \alpha_4(\beta_1 N_* \tau \hat{K}_i - \beta_1 N_* \hat{K}_p - \beta_3 \hat{K}_i), \\ r_{11} &= \alpha_4(\beta_1 N_* \hat{K}_p + \beta_3 \hat{K}_i + \hat{K}_v), \\ r_{12} &= -2\alpha_4 \hat{K}_v, \\ r_{13} &= \alpha_4 \hat{K}_v, \\ r_{20} &= \alpha_4(\beta_2 N_* \tau \hat{K}_i - \beta_2 N_* \hat{K}_p - \beta_4 \hat{K}_i), \\ r_{21} &= \alpha_4(\beta_2 N_* \hat{K}_p + \beta_4 \hat{K}_i). \end{aligned} \quad (31)$$

Using the notation $\theta_1 = \angle \Gamma_1(e^{j\omega\tau})$, $\theta_2 = \angle \Gamma_2(e^{j\omega\tau})$ and some trigonometrical identities, one may obtain the steady state

response

$$\begin{aligned} y_{ss}(k) &= v_L^{\text{amp}} |\Gamma_1(e^{j\omega\tau})| \sin((k-1)\omega\tau + \theta_1) \\ &\quad + v_L^{\text{amp}} |\Gamma_2(e^{j\omega\tau})| \cos((k-1)\omega\tau + \theta_2), \\ &= v_L^{\text{amp}} |\Gamma_{\text{cmp}}(e^{j\omega\tau})| \sin((k-1)\omega\tau + \psi), \end{aligned} \quad (32)$$

where

$$\begin{aligned} |\Gamma_{\text{cmp}}(e^{j\omega\tau})|^2 &= |\Gamma_1(e^{j\omega\tau})|^2 + |\Gamma_2(e^{j\omega\tau})|^2 \\ &\quad + 2\text{Im}(\Gamma_1(e^{j\omega\tau})\Gamma_2(e^{-j\omega\tau})), \end{aligned} \quad (33)$$

gives the square of the amplitude ratio and ψ is the phase lag.

Using (30) and (31), one may derive the string stability condition

$$|\Gamma_{\text{cmp}}(e^{j\omega\tau})|^2 = \frac{\sum_{m=0}^2 (N_m \cos(m\omega\tau))}{\sum_{m=0}^4 (D_m \cos(m\omega\tau))} < 1, \quad (34)$$

where the coefficients N_m and D_m are defined in Appendix B. This can be re-written as

$$\begin{aligned} g_1(\hat{K}_i, \hat{K}_p, \hat{K}_v, v^*, \tau; \omega) \\ = \sum_{m=0}^2 (N_m \cos(m\omega\tau)) - \sum_{m=0}^4 (D_m \cos(m\omega\tau)) < 0. \end{aligned} \quad (35)$$

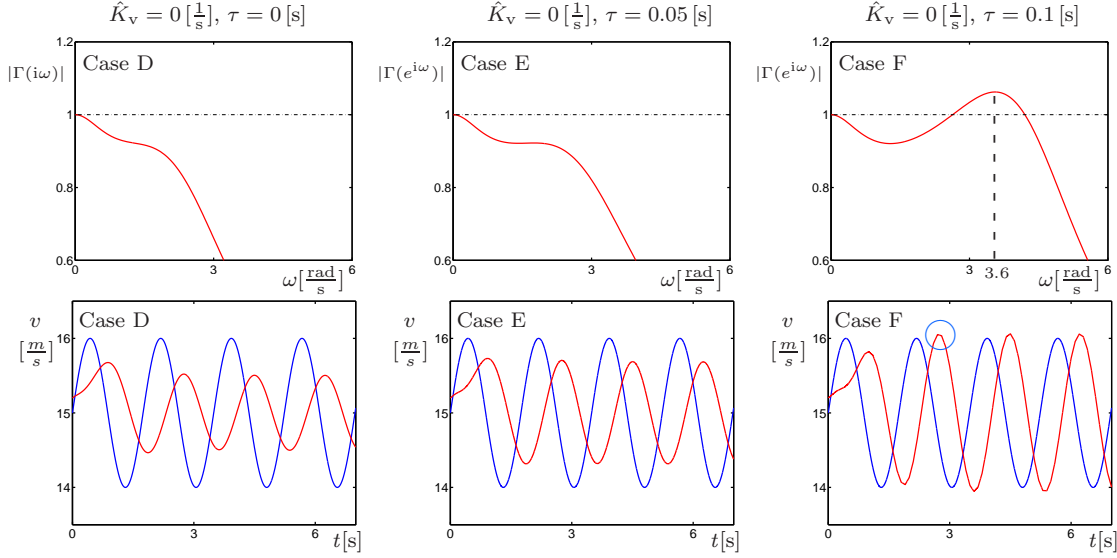


Figure 7. TOP ROW: OUTPUT-INPUT AMPLITUDE RATIOS AS A FUNCTION OF THE EXCITATION FREQUENCY ω CORRESPONDING TO THE POINTS D, E, AND F IN Fig. 4. BOTTOM ROW: SIMULATION RESULTS OF THE NONLINEAR SYSTEM (8) SUBJECT TO SINUSOIDAL INPUT (12) WITH $v_L^* = 15$ m/s, $v_L^{\text{amp}} = 1$ m/s, $\omega = 3.6$ rad/s. THE INITIAL CONDITIONS ARE $\tilde{h}_0 = 0.2$ m, $\tilde{v}_0 = 0.2$ m/s, $\tilde{e}_0 = 0$ m/s. BLUE AND RED CURVES REPRESENT THE LEADER'S AND FOLLOWER'S VELOCITIES, RESPECTIVELY.

In order to guarantee string stability, one needs to ensure that the maximum of $g_1(\hat{K}_i, \hat{K}_p, \hat{K}_v, v^*, \tau; \omega)$ is less than 0. Let us define

$$\begin{aligned} g_2(\hat{K}_i, \hat{K}_p, \hat{K}_v, v^*, \tau; \omega) &= \frac{d}{d\omega} g_1(\hat{K}_i, \hat{K}_p, \hat{K}_v, v^*, \tau; \omega) \\ &= \sum_{m=0}^2 \left(P_{1m} \cos(m\omega\tau) \right) + \sum_{m=1}^4 \left(P_{2m} \sin(m\omega\tau) \right), \end{aligned} \quad (36)$$

where the coefficients P_{1m} and P_{2m} are defined in Appendix B. Thus for $\omega > 0$, the string stability boundary is given by

$$\begin{cases} g_1(\hat{K}_i, \hat{K}_p, \hat{K}_v, v^*, \tau; \omega) = 0, \\ g_2(\hat{K}_i, \hat{K}_p, \hat{K}_v, v^*, \tau; \omega) = 0. \end{cases} \quad (37)$$

Similar to the plant stability analysis, we fix \hat{K}_v, v^* and τ to obtain string stability boundaries in the (\hat{K}_i, \hat{K}_p) parameter plane. It is not possible to get a closed-form solution for \hat{K}_i and \hat{K}_p as a function of ω from the transcendental parametric equation (37). One way to get a numerical solution is to create a mock differential equation

$$\begin{cases} \dot{\hat{K}}_i = g_1(\hat{K}_i, \hat{K}_p; \omega) \\ \dot{\hat{K}}_p = g_2(\hat{K}_i, \hat{K}_p; \omega) \end{cases} \quad (38)$$

and use numerical continuation [13] to track the equilibria of this system while changing the parameter $\omega > 0$. This requires an

initial guess for a chosen ω which can be corrected using the Newton-Raphson method and this can be repeated for nearby ω s using the corrected point as initial guess. Thus, the parametric representation of the string stability boundary can be obtained numerically.

One may show that $g_1(\hat{K}_i, \hat{K}_p, \hat{K}_v, v^*, \tau; 0) = 0$ and $g_2(\hat{K}_i, \hat{K}_p, \hat{K}_v, v^*, \tau; 0) = 0$, which means that $\omega = 0$ is always a local extremum. Consequently, at $\omega = 0$ string stability is given by $\frac{d^2}{d\omega^2} g_1(\hat{K}_i, \hat{K}_p, \hat{K}_v, v^*, \tau; 0) < 0$ which yields

$$\hat{K}_i > \frac{24N_*\alpha_0^3(e^{\alpha_0\tau} - 1)^2}{12N_*^2\alpha_0^2\tau^2e^{\alpha_0\tau} - (12N_*^2 - 12\alpha_0^2 + N_*^2\alpha_0^2\tau^2)(e^{\alpha_0\tau} - 1)^2}. \quad (39)$$

The string stability boundaries (37) and (39) are also plotted in Fig. 4 in the (\hat{K}_i, \hat{K}_p) -plane as solid blue curves for different values of \hat{K}_v and τ when $v^* = 15$ m/s. Dark gray lobe-shaped domains correspond to string stable behavior and these are embedded in the light gray plant stable domains. We remark that there exist another string stability boundary which is not shown in Fig. 4 as it is located in the white region where plant stability is violated. The string stable domain also shrinks when the sampling time τ is increased and at a critical value the domain disappears. Indeed, this critical delay depends on \hat{K}_v and our initial investigations suggest that it is the largest for $\hat{K}_v \approx N_*$ in which case it takes the value $\tau_{\text{cr}} \approx 1/(3N_*) = 0.212$ s. The critical angular frequency at which string stability changes is denoted by ω_{cr} and depicted in Fig. 5 corresponding to the string stability curves at the top row of Fig. 4. One may observe that

ω_{cr} increases monotonously along the string stability boundary and consequently string stability is lost in the low- and high-frequency ranges when crossing the lower and upper part of the string stability boundary, respectively.

To illustrate that string stability can be lost when increasing the sampling time τ , the point $(\hat{K}_i, \hat{K}_p) = (4, 4)$ is marked at the first three panels in Fig. 4, denoted by D, E and F, respectively. While the controller with these gains is string stable for the continuous-time system and for the discrete-time system with small sampling time ($\tau = 0.05$ s), it is string unstable for larger sampling time ($\tau = 0.1$ s). This can also be observed at the top row of Fig. 7 that the magnitude of the transfer function stays below 1 for zero and small τ but exceeds 1 in the mid-frequency regime for larger sampling time. Fig. 4 shows that the string stable domain increases monotonously with \hat{K}_v for the continuous-time system but for the discrete-time system the string stable domain may be shifted, expanded or shrunk while increasing \hat{K}_v , making control design non-trivial.

The amplification ratio obtained from the transfer function (34) and the time response of the nonlinear discrete-time system (8) are shown in Fig. 7 for points D, E and F when the system is subjected to a sinusoidal input (12). The frequency is chosen to be $\omega = 3.6$ rad/s where the transfer function reaches its maximum for $\tau = 0.1$ s; see top right panel in Fig. 7. Indeed, the time steps used for the simulations are much smaller than the sampling time τ . The region highlighted by a cyan circle on the rightmost panel in Fig. 7 emphasizes the non-smoothness caused by digital effects. Again, this shows that (relatively) small sampling times can significantly alter the system dynamics by causing instabilities.

CONCLUSIONS

In this paper we investigated the dynamics of digitally controlled connected vehicles that control their motion based on the signals received from the vehicle in front. By extending the notion of plant and string stability to the analogous discrete-time system we showed that the arising time-varying time delays introduced by the finite sampling time have a significant effects on the stability of vehicle flows. In particular, above a critical delay no gain combinations exist that can ensure string stability. While more sophisticated controllers may be designed, those will also possess similar limitations. In the future the authors are planning to extend the analysis for more complicated network structures arising in connected vehicle systems and investigate the nonlinear dynamics of these systems.

REFERENCES

- [1] Orosz, G., Wilson, R. E., and Stépán, G., 2010. "Traffic jams: dynamics and control". *Philosophical Transactions of the Royal Society A*, **368**(1928), pp. 4455–4479.
- [2] Ioannou, P. A., and Chien, C. C., 1993. "Autonomous intelligent cruise control". *IEEE Transactions on Vehicular Technology*, **42**(4), pp. 657–672.
- [3] Vahidi, A., and Eskandarian, A., 2003. "Research advances in intelligent collision avoidance and adaptive cruise control". *IEEE Transactions on Intelligent Transportation Systems*, **4**(3), pp. 143–153.
- [4] Caveney, D., 2010. "Cooperative vehicular safety applications". *IEEE Control Systems Magazine*, **30**(4), pp. 38–53.
- [5] Nowakowski, C., Shladover, S. E., and Cody, D., 2010. Cooperative adaptive cruise control: testing drivers' choices of following distances. Tech. rep., University of California, Berkeley.
- [6] Phillips, C. L., and Nagle, H. T., 1995. *Digital Control System Analysis and Design*, third ed. Prentice-Hall.
- [7] Stépán, G., 2001. "Vibrations of machines subjected to digital force control". *International Journal of Solids and Structures*.
- [8] Orosz, G., and Shah, S. P., 2012. "A nonlinear modeling framework for autonomous cruise control". In Proceedings of the ASME Dynamic Systems and Control Conference, ASME.
- [9] Swaroop, D., and Hedrick, J. K., 1996. "String stability of interconnected systems". *IEEE Transactions on Automatic Control*, **41**(3), pp. 349–357.
- [10] Ge, J. I., Avedisov, S. S., and Orosz, G., 2013. "Stability of connected vehicle platoons with delays acceleration feedback". In Proceedings of the ASME Dynamical Systems and Control Conference, ASME.
- [11] Zhang, L., and Orosz, G., 2013. "Designing network motifs in connected vehicle systems: delay effects and stability". In Proceedings of the ASME Dynamical Systems and Control Conference, ASME.
- [12] Zhao, X. M., and Orosz, G., 2013. "Nonlinear day-to-day traffic dynamics with driver experience delay: modeling, stability and bifurcation analysis". *Submitted*.
- [13] Roose, D., and Szalai, R., 2007. "Continuation and bifurcation analysis of delay differential equations". In Numerical Continuation Methods for Dynamical Systems, B. Krauskopf, H. M. Osinga, and J. Galan-Vioque, eds., Understanding Complex Systems, Springer, pp. 359–399.

Table 1. DATA OF A 2011 CHEVROLET HHR VEHICLE ARE SHOWN TOGETHER WITH THE PARAMETERS USED FOR THE RANGE POLICY [8].

$m = 1555 \text{ kg}$	mass of the vehicle
$C_d = 0.34$	air drag coefficient
$A = 2.3 \text{ m}^2$	frontal area
$\rho = 1.184 \text{ kg/m}^3$	air density at 25 °C
$k = \frac{1}{2}C_d\rho A = 0.463 \text{ kg/m}$	
$R = 0.313 \text{ m}$	tyre rolling radius
$\gamma = 0.011$	tyre rolling resistance coefficient
$g = 9.81 \text{ m/s}^2$	gravitational constant
$l = 5 \text{ m}$	vehicle length(approximation)
$v_{\max} = 30 \text{ m/s}$	desire maximum velocity
$h_{\text{st}} = 5 \text{ m}$	desired stopping distance
$h_{\text{go}} = 35 \text{ m}$	desired free flow distance

Appendix A: Parameters Used in The Paper

Appendix B: Coefficients Used in the Paper

In (25) and (26) the coefficients are defined by

$$\begin{aligned}
 b_{11} &= \frac{1}{2}(N_*\tau\alpha_3 - 2\alpha_1 + 2\alpha_2\alpha_4 - 2e^{-\alpha_0\tau}\alpha_1 + N_*\tau\alpha_4^2 + N_*\tau\alpha_3e^{-\alpha_0\tau}), \\
 b_{10} &= 2\alpha_4\hat{K}_v + 2 + 2e^{-\alpha_0\tau}, \\
 b_{23} &= -8\alpha_4 + 8\alpha_4^2N_* + 8\alpha_3N_*e^{-\alpha_0\tau}, \\
 b_{22} &= -4\alpha_3N_*e^{-2\alpha_0\tau} - (12\alpha_3N_* + 4\alpha_4^2N_* - 4\alpha_4)e^{-\alpha_0\tau} \\
 &\quad + 16\alpha_4 - 12\alpha_4^2N_* - 4\alpha_3N_*, \\
 b_{21} &= 6\alpha_3N_*e^{-2\alpha_0\tau} + (2\alpha_3\alpha_4N_*\hat{K}_v + 4\alpha_3N_* + 6\alpha_4^2N_* - 8\alpha_4)e^{-\alpha_0\tau} \\
 &\quad + 6\alpha_3N_* + 2\alpha_4^3N_*\hat{K}_v + 2\alpha_4^2N_* - 8\alpha_4 - 2\alpha_3\alpha_4N_*\hat{K}_v, \\
 b_{20} &= -2\alpha_3N_*e^{-2\alpha_0\tau} + (4\alpha_4 - 2\alpha_3\alpha_4\hat{K}_vN_* - 2\alpha_4^2N_*)e^{-\alpha_0\tau} \\
 &\quad + 2\alpha_4^2N_* - 2\alpha_3N_* + 2\alpha_3\alpha_4\hat{K}_vN_* - 2\alpha_4^3\hat{K}_vN_*, \\
 b_{33} &= (8N_*\tau\alpha_3 - 8\alpha_1)e^{-\alpha_0\tau} + 8\alpha_2\alpha_4 + 8N_*\tau\alpha_4^2, \\
 b_{32} &= (4\alpha_1 - 4N_*\tau\alpha_3)e^{-2\alpha_0\tau} - (4N_*\tau\alpha_4^2 + 8N_*\tau\alpha_3 + 4\alpha_2\alpha_4 \\
 &\quad - 12\alpha_1)e^{-\alpha_0\tau} - 8N_*\tau\alpha_4^2 + 4\alpha_1 - 4N_*\tau\alpha_3 - 12\alpha_2\alpha_4, \\
 b_{31} &= (4N_*\tau\alpha_3 - 6\alpha_1)e^{-2\alpha_0\tau} + (4N_*\tau\alpha_4^2 - 2\alpha_1\alpha_4\hat{K}_v + 2\alpha_3\alpha_4N_*\tau\hat{K}_v \\
 &\quad - 4\alpha_1 + 6\alpha_2\alpha_4)e^{-\alpha_0\tau} + 4N_*\tau\alpha_3 + 2\alpha_4^3N_*\tau\hat{K}_v + 2\alpha_2\alpha_4^2\hat{K}_v \\
 &\quad + 2\alpha_2\alpha_4 + 2\alpha_1\alpha_4\hat{K}_v - 2N_*\tau\alpha_4^2 - 6\alpha_1, \\
 b_{30} &= 2e^{-2\alpha_0\tau}\alpha_1 - (2\alpha_3\alpha_4N_*\tau\hat{K}_v - 2\alpha_1\alpha_4\hat{K}_v + 2\alpha_2\alpha_4)e^{-\alpha_0\tau} \\
 &\quad + 2N_*\tau\alpha_4^2 + 2\alpha_2\alpha_4 - 2\alpha_4^3N_*\tau\hat{K}_v + 2\alpha_1 - 2\alpha_1\alpha_4\hat{K}_v - 2\alpha_2\alpha_4^2\hat{K}_v,
 \end{aligned} \tag{40}$$

and by

$$\begin{aligned}
 d_{10} &= -2\alpha_4 + \alpha_4^2N_* + \alpha_3e^{-\alpha_0\tau}N_* + \alpha_3N_*, \\
 d_{21} &= (-2N_*\tau\alpha_3\alpha_4 + 2N_*^2\tau\alpha_3^2 + 2\alpha_4\alpha_1)e^{-\alpha_0\tau} + 2N_*^2\tau\alpha_4^2\alpha_3 \\
 &\quad - 2\alpha_2\alpha_4^2 - 2\alpha_4\alpha_1 + 2\alpha_4^2N_*\alpha_1 + 2\alpha_2\alpha_4\alpha_3N_* - 2N_*\tau\alpha_4^3, \\
 d_{20} &= -N_*^2\tau\alpha_3^2e^{-2\alpha_0\tau} - (2N_*^2\tau\alpha_4^2\alpha_3 - 2N_*\tau\alpha_3\alpha_4 + 2\alpha_1\alpha_4)e^{-\alpha_0\tau} \\
 &\quad - 2\alpha_2\alpha_4\alpha_3N_* + 2\alpha_2\alpha_4^2 + 2\alpha_1\alpha_4 + 2N_*\tau\alpha_4^3 \\
 &\quad - 2\alpha_1\alpha_4^2N_* - N_*^2\tau\alpha_3^2 - N_*^2\tau\alpha_4^4,
 \end{aligned} \tag{41}$$

where α_i are defined by (17).

In (34) and (35), the coefficients are defined by

$$\begin{aligned}
 N_0 &= \frac{6\alpha_4^2N_*(N_*\hat{K}_1^2 + N_*\omega^2\hat{K}_p^2 - 2\omega^2\hat{K}_i\hat{K}_v)}{\omega^4} + 6\alpha_4^2\hat{K}_v^2, \\
 N_1 &= -\frac{8\alpha_4^2N_*(N_*\hat{K}_1^2 + N_*\omega^2\hat{K}_p^2 - 2\omega^2\hat{K}_i\hat{K}_v)}{\omega^4} - 8\alpha_4^2\hat{K}_v^2, \\
 N_2 &= \frac{2\alpha_4^2N_*(N_*\hat{K}_1^2 + N_*\omega^2\hat{K}_p^2 - 2\omega^2\hat{K}_i\hat{K}_v)}{\omega^4} + 2\alpha_4^2\hat{K}_v^2,
 \end{aligned} \tag{42}$$

and by

$$\begin{aligned}
 D_0 &= a_3^2 + a_2^2 + a_1^2 + a_0^2 + 1, \\
 D_1 &= 2(a_1a_2 + a_2a_3 + a_3 + a_0a_1), \\
 D_2 &= 2(a_1a_3 + a_2 + a_0a_2), \\
 D_3 &= 2(a_1 + a_0a_3), \\
 D_4 &= 2a_0,
 \end{aligned} \tag{43}$$

where α_i are defined in (17) and a_i are defined in (20).

In (36), the coefficients are defined by

$$\begin{aligned}
 P_{10} &= \frac{12\alpha_4^2N_*}{\omega^5}(2N_*\hat{K}_1^2 + N_*\omega^2\hat{K}_p^2 - 2\omega^2\hat{K}_i\hat{K}_v), \\
 P_{11} &= -\frac{16\alpha_4^2N_*}{\omega^5}(2N_*\hat{K}_1^2 + N_*\omega^2\hat{K}_p^2 - 2\omega^2\hat{K}_i\hat{K}_v), \\
 P_{12} &= \frac{4\alpha_4^2N_*}{\omega^5}(2N_*\hat{K}_1^2 + N_*\omega^2\hat{K}_p^2 - 2\omega^2\hat{K}_i\hat{K}_v), \\
 P_{21} &= -\frac{8\tau\alpha_4^2N_*}{\omega^4}(N_*\hat{K}_1^2 + N_*\omega^2\hat{K}_p^2 - 2\omega^2\hat{K}_i\hat{K}_v) - 8\tau\alpha_4^2\hat{K}_v^2 \\
 &\quad - 2(a_0a_1 + a_1a_2 + a_2a_3 + a_3)\tau, \\
 P_{22} &= \frac{4\tau\alpha_4^2N_*}{\omega^4}(N_*\hat{K}_1^2 + N_*\omega^2\hat{K}_p^2 - 2\omega^2\hat{K}_i\hat{K}_v) + 4\tau\alpha_4^2\hat{K}_v^2 \\
 &\quad - 4(a_1a_3 + a_0a_2 + a_2)\tau, \\
 P_{23} &= -6(a_0a_3 + a_1)\tau, \\
 P_{24} &= -8a_0\tau,
 \end{aligned} \tag{44}$$

where α_i are defined in (17) and a_i are defined in (20).